Intertwined orbital distribution of charge density waves in $NbSe_2$

Jyun-Yu Wu,[1] Yung-Ting Lee,[2,3] Guan-Hao Chen,[1,4] Zheng-Hong Li,[1] Chang-Tsan Lee,[1] Jie-Yu Hsu,[1] Chia-Nung Kuo,[5] Juhn-Jong Lin,[1] Wen-Hao Chang,[1,4] Chin Shan Lue,[5,6] Noriaki Takagi,[7] Po-Tuan Chen,[2] Cheng-Tien Chiang,[8,9] Chien-Cheng Kuo,[10] Chien-Te Wu,[1,11] Chi-Cheng Lee,[9,*] Ming-Chiang Chung,[12,†] Hung-Chung Hsueh,[9,‡] and Chun-Liang Lin[1,§]

[1]*Department of Electrophysics, National Yang Ming Chiao Tung University, Hsinchu 300, Taiwan*
[2]*Department of Vehicle Engineering, National Taipei University of Technology, Taipei 106, Taiwan*
[3]*Department of Applied Science, National Taitung University, Taitung 950309, Taiwan*
[4]*Research Center for Applied Sciences, Academia Sinica, Taipei 115, Taiwan*
[5]*Department of Physics, National Cheng Kung University, Tainan 701, Taiwan*
[6]*Taiwan Consortium of Emergent Crystalline Materials, National Science and Technology Council, Taipei 106, Taiwan*
[7]*Graduate School of Human and Environmental Studies, Kyoto University, Kyoto 606-8501, Japan*
[8]*Institute of Atomic and Molecular Sciences, Academia Sinica, Taipei 106, Taiwan*
[9]*Department of Physics, Tamkang University, New Taipei 251, Taiwan*
[10]*Department of Physics, National Sun Yat-Sen University, Kaohsiung 804, Taiwan, Taiwan*
[11]*Physics Division, National Center for Theoretical Sciences, Taipei, 106, Taiwan*
[12]*Department of Physics, National Chung Hsing University, Taichung 402, Taiwan*

(Received 31 January 2024; accepted 18 September 2025; published 21 November 2025; corrected 15 December 2025)

Charge density wave (CDW) resulting from a periodic distortion in the lattice creates orders beyond the original lattice. In $2H$-$NbSe_2$, one of the layered transition metal dichalcogenides, the 3×3 charge order appears in two-dimensional (2D) layers. Although CDW can be observed by different techniques, the spatial distribution within a 2D layer has never been systematically visualized. Here, by using scanning tunneling microscopy and density functional theory, we monitored the evolution of CDW along the c axis and found a strong relation with the orbital charges. The results show that the appearance of the CDW varies while tuning the tunneling current and undergoes a transition from Se orbital charges to Nb orbital charges. The calculation of orbital charge distributions shows that both CDW intensity modulation and the transition are strongly intertwined with the distribution of Se $4p$ orbitals and Nb $4d$ orbitals.

DOI: 10.1103/dn1j-gkjs

I. INTRODUCTION

Charge density wave (CDW) arising from Peierls transition can create a new order inside crystals [1]. Influenced by the new order, several macroscopic properties similar to superconductivity can be observed. For example, the nonlinear changes of resistivity in crystals are observed in temperature-dependent transport measurements [2,3], and Fermi surface nesting is revealed by angle-resolved photoelectron spectroscopy below transition temperature [4,5]. From a microscopic point of view, the new order of the charge density is strongly and spontaneously related to the periodic displacement of atoms in the lattice. The periodic displacements in the CDW phase can be observed by several techniques, such as X-ray diffraction [2,6], Raman spectroscopy [7,8], and high-resolution transmission electron microscopy [9,10]. On the other hand, scanning tunneling microscopy (STM) usually provides real-space distributions of charge orders at the surface level [11,12]. In some of the cases like $NbSe_2$, the CDW is caused by a main contribution from the horizontal displacement of inner Nb atoms and a relatively minor effect of the vertical displacement of surface Se atoms [13,14]. Therefore, observing the distributions of charge orders at the Nb level can further clarify the relationship between the CDW and the displacement of each atom. Especially, the difference between variant phases (i.e., hollow or filled) is closely associated with the displacement of Nb atoms. For $2H$-$NbSe_2$, it shows 3×3 CDW below 35 K in bulk crystal [15], and T_{CDW} can be further enhanced to 145 K for monolayer [16]. On the other hand, CDW and superconductivity can coexist in $2H$-$NbSe_2$ bulk up to 7.2 K [17]. A former study has visualized the layer-dependent superconducting properties of $2H$-$NbSe_2$ [15], but the distribution of CDW along the c axis has not been visualized yet.

STM is a suitable method to visualize CDW because of its sub-ångström resolution. Not only for conventional CDW in layer materials [18–21], the relationship between

*Contact author: cclee.physics@gmail.com
†Contact author: mingchiangha@phys.nchu.edu.tw
‡Contact author: hchsueh521@gmail.com
§Contact author: clin@nycu.edu.tw

Published by the American Physical Society under the terms of the Creative Commons Attribution 4.0 International license. Further distribution of this work must maintain attribution to the author(s) and the published article's title, journal citation, and DOI.

unconventional charge orders or even pair density wave and lattice geometry in Kagome materials such as AV_3Sb_5 (A = K, Cs, Rb) can also be identified [22–24]. For $NbSe_2$, many previous studies have shown the evolution of CDW along the energy level by tuning the sample bias [25–29], especially a multiband feature can strongly affect the apparent phase of CDW [29]. Yet, there has been a fierce debate on whether CDW in $NbSe_2$ is caused by Peierls-like weak coupling or strong electron-phonon coupling, which cannot be explained by the energy-dependent evolution of the CDW. Several recent works indicate that the orbital order inside the layered structure and its relation with CDW can provide key information to this issue [30,31]. Here, by tuning the tunneling current, STM allows us to probe the distribution of charge density at different heights within a layer [32]. It is found that the apparent corrugation of the 3×3 charge order exhibits a strong dependence on the tunneling current, i.e., tip-sample distance, in both filled and hollow configurations. By comparing with the 1×1 atomic lattice, the 3×3 charge order relatively becomes weaker with the tip approaching, but it turns stronger after a certain set point. Hereby, it is possible to reveal that the distribution of the CDW is inhomogeneous along the c axis. Furthermore, we clearly identify the detailed evolution of spatial distribution via probing the 3×3 charge order at Se and Nb sublayer. The results are reproduced by the simulation based on density functional theory (DFT), further confirming that the appearance of CDW is strongly intertwined with the orbital charge distribution inside the crystal.

II. METHODS

A. Sample preparation and STM characterization

The single crystal $2H$-$NbSe_2$ was introduced into the UHV chamber at a base pressure of 2×10^{-10} torr and *in situ* cleaved. The STM measurements were performed under liquid He conditions and the actual temperature is 4.8 K in the Scienta Omicron LT-STM and 10.2 K in INFINITY SPM. STM tip was made of tungsten that was prepared by electrochemical etching in the 3M NaOH solution.

B. Theoretical calculation based on DFT

Based on DFT, norm-conserving pseudopotentials, and optimized pseudoatomic basis functions, the first-principles calculations of the $NbSe_2$ materials were calculated by using the OPENMX (3.9.9) code [33–38]. The generalized gradient approximation was used in the Perdew-Burke-Ernzerhof scheme [39] to treat the exchange-correlation function. The optimized radial functions, Nb-s3p2d2 and Se-s3p2d2, were used for niobium and selenium, respectively, where the abbreviations of the basis functions represent (atomic symbol) − (number of radial functions for s, p, and d orbitals). In DFT calculations, the criterions of force convergence and electronic self-consistent field were set to 10^{-4} hartree/bohr and 10^{-8} hartree, respectively. The k grid in the $NbSe_2$ $3 \times 3 \times 1$ monolayer was set to $9 \times 9 \times 1$. The energy cutoff was 600 Ry. The Tersoff-Hamann scheme was employed to simulate STM images with partial charge density [40]. The $NbSe_2$ structures and charge density iso-surfaces are plotted by using VESTA [41] and OPENMX Viewer [42], respectively. The thickness of a single $NbSe_2$ layer is 6.8 Å in the simulation.

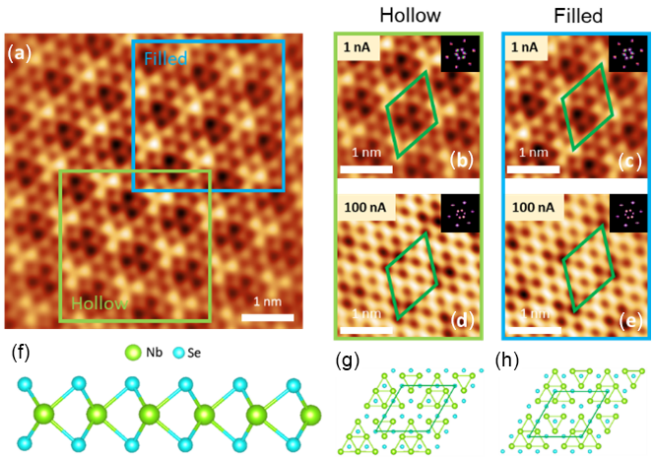


FIG. 1. Current-dependent STM images of hollow and filled phase of $2H$-$NbSe_2$. (a) The STM image of $2H$-$NbSe_2$ acquired at 1 nA simultaneously shows two types of CDW phases, hollow and filled, marked with green and blue square frames, respectively. (b), (c) Typical STM images of hollow and filled phases cut from panel (a), respectively. (d), (e) STM images of hollow and filled phase acquired at the same position as panels (b) and (c) but at 100 nA, respectively. The rhombic 3×3 supercells of hollow and filled phases are indicated in green. The insets at the right-up corner of (b)–(e) show FFT images of each topography. All the FFT images show the 1×1 Bragg peaks and the 3×3 CDW signal. All the STM images are acquired at the sample bias of −10 mV. (f) The side view of atomic model of a single $2H$-$NbSe_2$ layer. (g), (h) Top view of CDW atomic models of hollow and filled phases, respectively.

III. RESULTS AND DISCUSSION

A. Current-dependent STM images of $2H$-$NbSe_2$

For the 3×3 CDW in $2H$-$NbSe_2$, several different atomic configurations are observed [15,27,43,44]. The filled and hollow phases as described in Fig. 1 are two configurations mostly observed in the STM experiments [15,27]. The difference in these two configurations is mainly due to the different rearrangements of Nb atoms. Figure 1(a) shows the STM image of an *in situ* cleaved $2H$-$NbSe_2$ surface, and both the 1×1 atomic lattice and 3×3 charge order are observed. Similar to several previous researches [15,27], two different phases can be found simultaneously. One is the "hollow" phase as indicated by the green square and the other is the "filled" phase as indicated by the blue square. In both phases, the CDW lattice distortion with rearranged Nb atomic positions is mainly driven by the electron-phonon coupling. As shown in Figs. 1(g) and 1(h), triangular clustering of Nb atoms forms big hexamer (six Nb) and small trimer (three Nb) triangles, which are empty at the center for the hollow phase but filled with an Se atom for the filled phase. The difference can also be observed in STM images. At −10 mV sample bias, the hollow phase is observed as bright three-pointed stars derived from the Se atoms on the top of Nb trimer as shown in Fig. 1(b). On the other hand, the filled phase is seen as bright spots associated with an Se atom on the center of Nb hexamer as shown in Fig. 1(c). According to the fast Fourier transform (FFT) images, both phases show primary 3×3 CDW wave vectors presented together with the Bragg vectors of 1×1 atomic lattice as shown in the insets of Figs. 1(b) and 1(c).

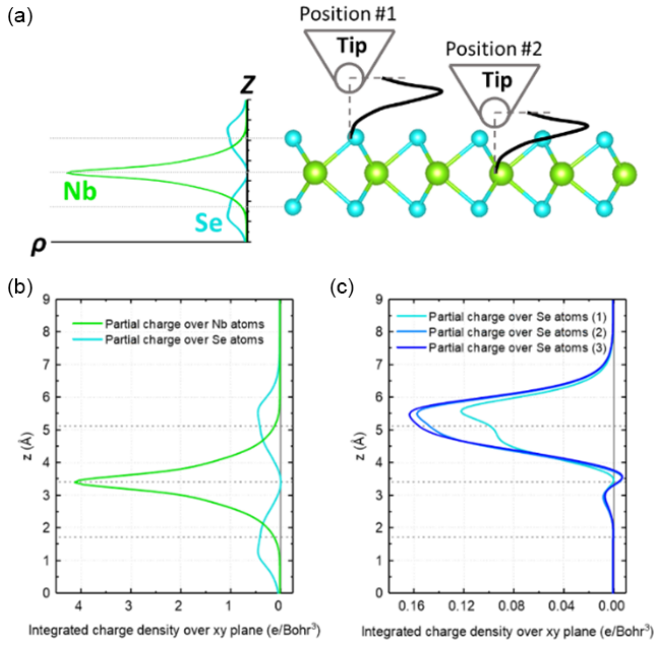


FIG. 2. Charge density distribution of Se and Nb along the c axis. (a) The illustration of how different states of Nb and Se atoms be acquired at different tip heights. The charge density of Nb and Se atoms decays into the vacuum and can be probed by the tip at different heights. The gray dashed line indicated the height level of atoms. The black curve represents the charge density distribution of an atom at the tip's apex. (b) The calculated charge density of Nb and Se atoms of $NbSe_2$ along the c axis. (c) The calculated charge density of Se atoms on three different sites at the topmost layer of $NbSe_2$.

Interestingly, while the tunneling current is increased from 1 to 100 nA, different apparent images can be obtained as shown by Figs. 1(d) and 1(e) for hollow and filled phases, respectively. It is well known that the distance between the tip and the sample in the STM tunneling junction can be tuned by the set point of tunneling currents. Thereby, it allows us to probe the corresponding real-space distribution of density of states (DOS) at different depths with respect to the outermost surface [32]. The higher value of the tunneling current, the deeper level is probed. As proved by our I-Z measurement shown in Fig. S1 [45], the tip gets closer to the sample by about 1.7 Å when the current increases from 1 to 100 nA. This displacement of the tip is close to the height difference between the topmost Se and Nb layer as shown in Fig. 2, which will be illustrated in the later section. Although the periodicity of both atomic lattices and charge orders remains the same as indicated by the FFT insets in Figs. 1(d) and 1(e), the intensity may vary as previously predicted for a similar transition metal dichalcogenide (TMD) material, NbS_2 [18]. As will be shown in the following, a systematic investigation can greatly help to understand the evolution of 3×3 charge order along the c axis from Se level to Nb level by tuning the set points of the tunneling current.

B. Explanation of current-dependent STM images

As known in the mechanism of STM imaging, the tip probes the states that decay gradually from the sample through the vacuum. Also, it is known that the tip is getting closer to the sample while increasing the tunneling current. Additionally, based on Tersoff-Hamann's theory, the contrast of the STM image is related to the charge density distribution, i.e., local density of states (LDOS), decaying to the position of the tip's apex [40]. When the tip is getting close to the sample surface, the tip can detect variable signals based on the charge density distribution. This tunneling current-dependent STM measurement has been previously used to visualize the surface-assisted orbital order on $CeCoIn_5$ [32]. Furthermore, the tip itself also has charge density decaying from its apex. This decaying charge density from the tip can couple with the charge density decaying from the sample to form the tunneling signal. This means the probing endpoint of the tip is a little bit away from its apex. As for this probing length, it depends on the decay length of the apex atom's states of the tip. (The element of our tip is tungsten, whose decay length is approximately 3 Å, as shown in Fig. S2 in the Supplemental Material.) In other words, the tip is able to probe deeper beneath the surface with subatomic order. From these points of view, the difference in STM images observed with different tunneling currents might be due to probing different charge densities decaying from Nb and Se atoms separately at various tip-sample distances (or tip height), as illustrated in Fig. 2(a).

To prove this hypothesis, we calculated the charge density distribution along the c axis, as shown in Figs. 2(b) and 2(c). In Fig. 2(b), the charge densities of both Nb and Se atoms decay out of the sample surface into the vacuum ($z > 5.11$ Å). Therefore, these states can overlap with the wave function of the tip and be detected as shown in Fig. 2(a). (Noticed that although a small portion of Nb states can be detected at position #1, the charge density of Se is still greater than Nb, resulting in the contrast in the observed STM images being mainly related to Se atoms.) When the tip is positioned at different heights, as shown on the right of Fig. 2(a), it probes different magnitudes of states decaying from Nb and Se atoms, resulting in contrast changes in STM images. Interestingly, at position #2, because of the decay length of the apex atom of the tip, the tip can probe the charge density of Nb more. On the other hand, as shown in Fig. 2(b), the charge density of Nb is much stronger because the outermost shell of Nb contains more electrons (d orbital) than that of Se. Figure 2(c) further shows the charge distribution of the topmost Se atoms in $NbSe_2$ with CDW. It indicates the charge distribution on three different sites of Se atoms in a 3×3 supercell is altered. The corresponding relation with Se sites can be seen in Fig. S3 in the Supplemental Material [45]. This altered charge distribution is the main reason that the 3×3 CDW order on the $NbSe_2$ surface can be observed. It also means that the appearance of the STM image is related to the charge density distribution. In order to provide more details, the STM images observed by gradually approaching tip to surface are presented.

C. Current-modulated 3 × 3 CDW intensity

Figure 3 summarizes all STM images obtained from 0.1 to 100 nA at both +10 and −10 mV sample biases focusing on the hollow phase. Similar experiments are performed for the filled phase and the results are presented in Fig. S4 in the Supplemental Material. Similar to the previous work done by Sivakumar *et al.*, both the 3×3 charge order and 1×1 lattice

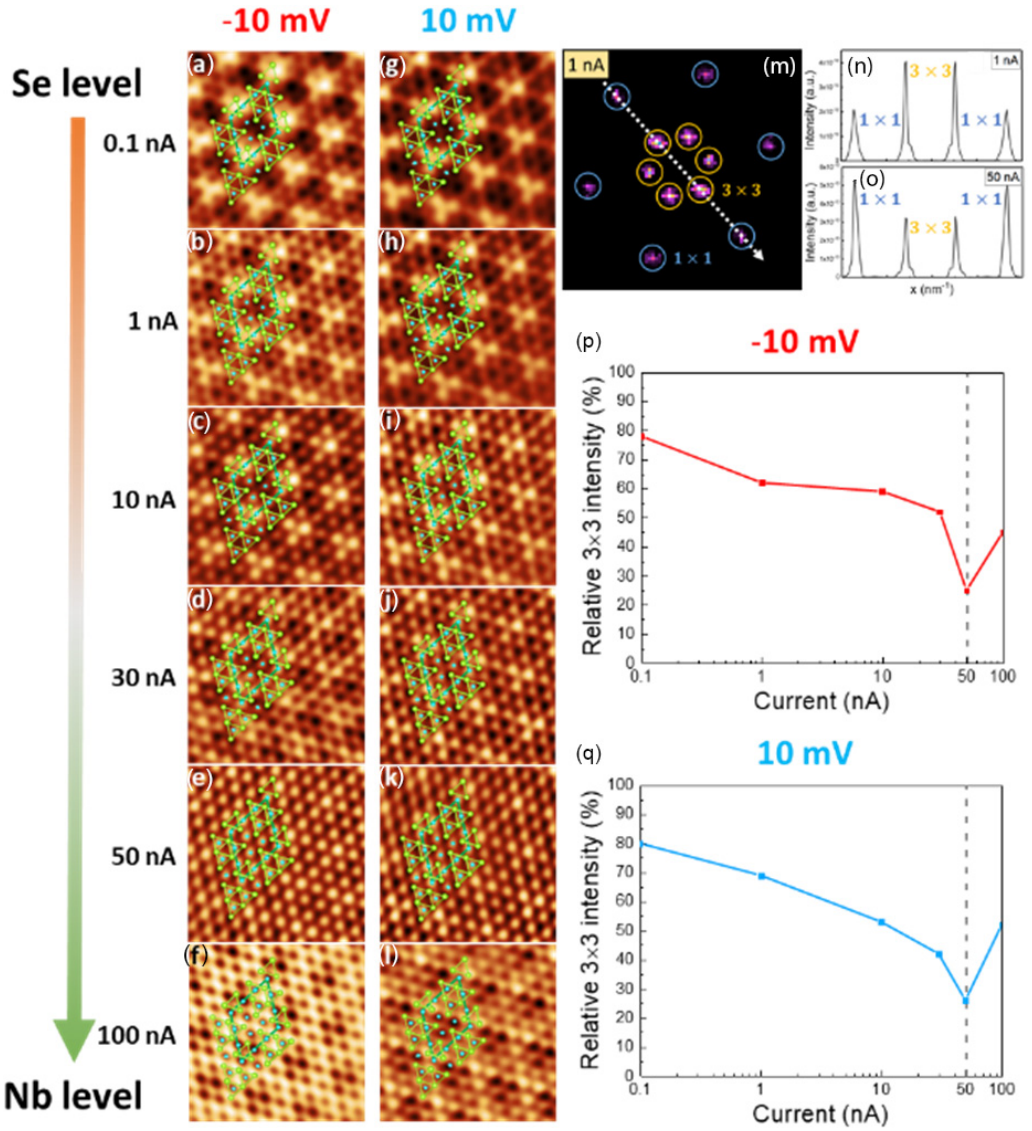


FIG. 3. Current-modulated 3 × 3 CDW intensity of hollow phase. Panels (a)–(f) and (g)–(l) are series of current-dependent STM images of hollow phase acquired from 0.1 to 100 nA at the sample bias of −10 and +10 mV, respectively. Atomic models of hollow phase are overlapped on panels (a)−(l) to indicate the locations of Nb and Se atoms. (m) The illustration of the method of acquiring the intensity of the 1 × 1 and the 3 × 3 peaks from the FFT image. Panels (n) and (o) are profiles acquired at 1 and 50 nA, respectively, using the line-profile analytical method illustrated in panel (m). (p), (q) The current-dependent evolution of the relative 3 × 3 intensity at −10 and +10 mV, respectively.

can be observed at all probed tip-surface distances [46]. It can be seen that the 3 × 3 charge order is clearly visible at 0.1 nA, but its signature gradually becomes weaker as the tunneling current increases. It is because the tip can gain more charge density when the tip is approaching, resulting in the intensity of 1 × 1 order becoming relatively greater than that of 3 × 3 order. Interestingly, although the 3 × 3 charge order almost disappears at 50 nA, it reappears with a different appearance at 100 nA. To explain this phenomenon, by overlapping the atomic models with the STM images as shown in Figs. 3(a)−3(f) and 3(g)−3(l), we can understand that the Se sites evolve from bright to dark dots from 50 to 100 nA, and Nb sites evolve from dark to bright simultaneously. This indicates that the STM tip starts to probe the DOS of Nb atoms gradually, and its magnitude becomes greater than the DOS of Se atoms from 50 to 100 nA, leading to the contrast inversion in STM images. (According to Fig. 2(b), it is possible that the Nb charge density is higher than that of Se.) Besides, this point implies that the CDW observed at 100 nA is mainly contributed by Nb atoms, different from the cases that are lower than 50 nA, which is mainly contributed by top Se atoms. This is also the reason why the spatial distributions of CDW observed at 1 and 100 nA as shown in Figs. 4(c) and 4(d), respectively, are distinct. In order to quantitatively understand the evolution of STM data as tuning tunneling currents, the intensity of FFT patterns corresponding to both the 1 × 1 Bragg spots and the 3 × 3 CDW is analyzed as shown by Fig. 3(m). The change in intensity along the white arrow in Fig. 3(m) is shown in Figs. 3(n) and 3(o). It is clear that the intensity of 3 × 3 peaks is stronger than 1 × 1 at 1 nA but becomes weaker than 1 × 1 at 50 nA. Figures 3(p) and 3(q) show the full evolutions for −10 and +10 mV

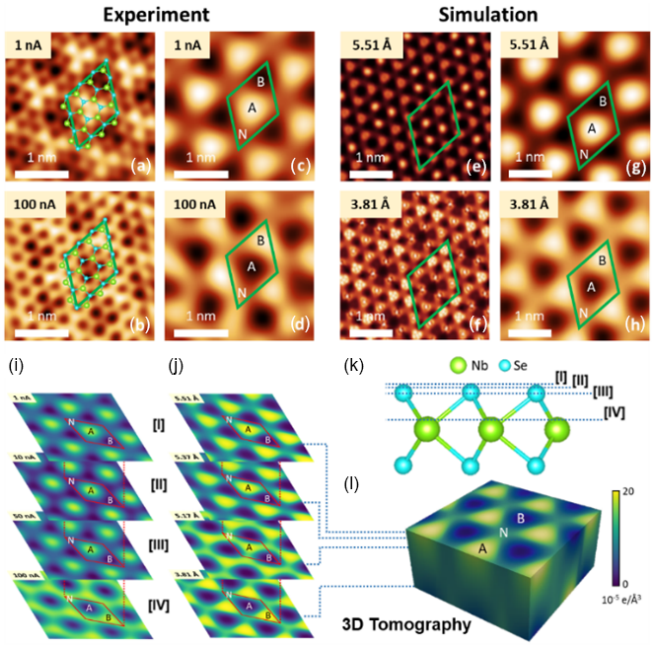


FIG. 4. Comparison of 3×3 CDW between experiment and simulation. (a), (b) STM images of the hollow phase at 1 and 100 nA, respectively. (c), (d) Extracted images highlight CDW signal, which are generated from panels (a), (b), respectively. (e), (f) Simulated STM images of the hollow phase at the surface (5.51 Å) and a deeper position (3.81 Å) of $NbSe_2$, respectively. (g), (h) Fourier-extracted images of CDW signal only, which are acquired from panels (e), (f), respectively. (i) Experimental results by different tunneling currents. Three different sites, A, B, and N are marked for identification of the change in intensity. (j) DFT simulated results at different heights. (k) Illustration of the scanning levels within a $NbSe_2$ layer. (l) Real-space three-dimensional (3D) spatial distribution of the CDW based on the theoretical simulation.

sample biases, respectively. The relative intensity ratios at different tunneling currents are calculated by the formula given below:

$$R_{3\times3} = I_{3\times3}/(I_{3\times3} + I_{1\times1}) \times 100\%. \quad (1)$$

By this quantification, the intensity evolution of both 3×3 and 1×1 order, and the turning points at 50 nA can be visualized more straightforwardly [as shown in Figs. 3(p) and 3(q)]. These experimental results can be supported by the DFT calculation in Fig. S5 in the Supplemental Material, and it indicates that the CDW distributes nonuniformly along the c axis within a single layer.

These results show that not only the choice of bias voltage matter, but the magnitude of the current is important as well when measuring $NbSe_2$ or other CDW systems by STM. Both parameters determine what information will be obtained, which may also affect the judgment of structural phases, especially when compared to DFT calculations. This is a noticeable point that should be carefully examined in other CDW systems.

D. Comparison of 3 × 3 CDW between STM observation and DFT calculations

To fully understand the evolution observed by current-dependent STM studies, we further compared them with the simulation by DFT calculations. Figures 4(a) and 4(b) are the STM images of the hollow phase acquired at 1 and 100 nA, respectively, at the same location. Figures 4(c) and 4(d) are images where FFT method is applied to extract the 3×3 charge order from Figs. 4(a) and 4(b), respectively. By extracting out only the charge order information, it can be clearly seen that the A site at 1 nA is the brightest but the B site becomes the brightest at 100 nA, while the N site remains the second bright region. It indicates that the distribution of two-dimensional CDW is not uniform along the c axis. Figures 4(e) and 4(f) are the DFT-simulated STM images cut at the height of 5.51 and 3.81 Å, respectively. (The average height of the bottom Se atoms is 2.11 Å.) Note that the height here is defined according to the distance from the bottom Se atoms toward the positive c axis. Although the height difference between 5.51 and 3.81 Å is 1.7 Å, which can well correspond to the tip displacement when changing current from 1 to 100 nA, the corresponding height of probing level is not linearly dependent on the logarithm of tunneling current. It implies that the overlapping of tip and sample wave functions should be considered. Even though the tip is approaching the sample from 1 to 50 nA, the probing level remains on the height as shown in Fig. 4(k), where the charge density of Se is relatively high. As a result, Fig. 4(e) is located closely to the outermost Se level, while Fig. 4(f) is located closer to the level of middle Nb atoms. Similarly, by filtering the lattice information, Figs. 4(g) and 4(h) highlight the 3×3 charge order from the simulated images near the Se and Nb levels, respectively. The apparent contrast inversion between A and B sites can also be observed in the simulated images, manifesting a spatial evolution of the CDW within a single layer $NbSe_2$. Figure 4(i) further shows four STM images obtained by tuning the tunneling currents. Figure 4(j) shows resembling tomography scans simulated at different height levels as labeled from [I] to [IV], respectively. The corresponding height levels of [I]–[IV] are illustrated in Fig. 4(k) and also identified in Fig. 4(l). Figure 4(l) visualizes the spatial distribution by integrating the constant-height STM images by DFT simulation. Furthermore, by changing the partial charge density (proportional to the current I), the constant-current STM images (shown in Figs. S12 and S13 in the Supplemental Material) correspond well with experimental results. The overall agreement between experiments and calculations clearly indicates that the spatial distribution of CDW is intertwined with the orbital contribution from the elements inside the crystal.

Furthermore, usually, the CDW revealed by the calculated charge density distribution is difficult to be verified by experiments directly. Here, the resemblance between the simulated STM images within the Tersoff approximation and the experimental STM results demonstrates such a possibility that the Tersoff approximation-based DFT simulation, where the partial charge density is calculated, can be used to complement the STM images in layered CDW systems.

E. Effect of electric field in the tunneling junction

In fact, increasing the tunneling current may not only probe the subsurface but also generate a larger electric field in between the tip and sample simultaneously. In our experiments,

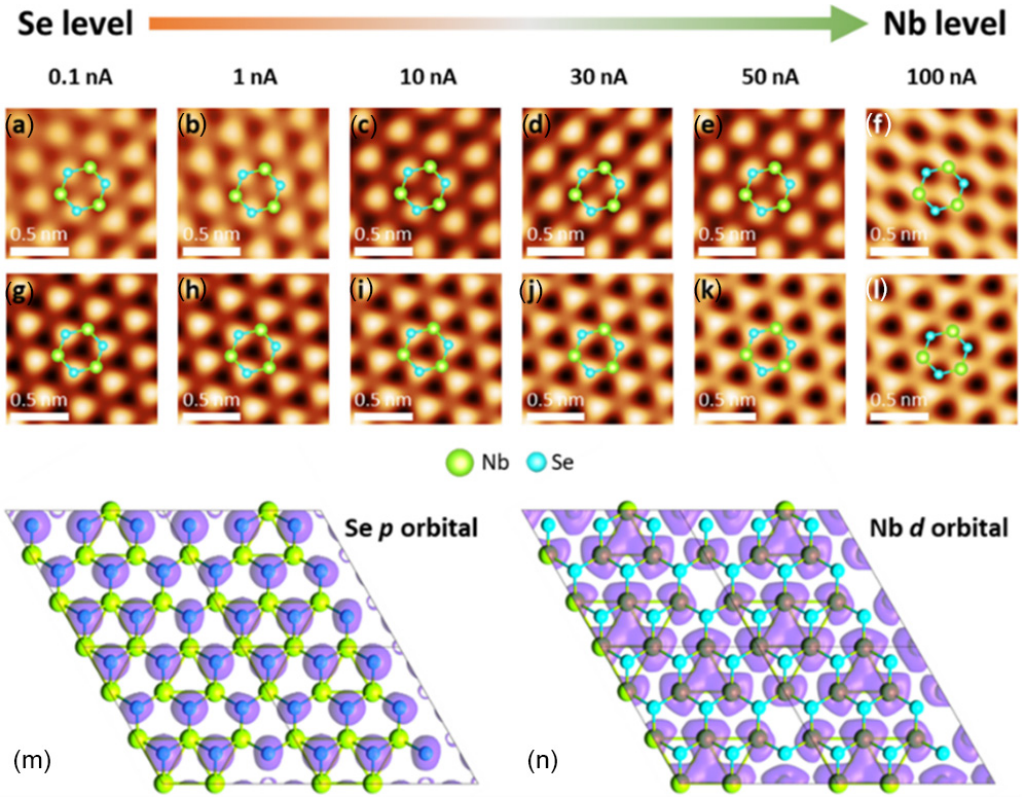


FIG. 5. Spatial distribution of orbital charges. (a)–(f) A series of Fourier-extracted STM images of 1×1 signal only, which are acquired from 0.1 to 100 nA. (g)–(l) A series of Fourier-extracted simulated images of 1×1 signal only, which represent orbital distributions from Se to Nb levels. Atomic models of $NbSe_2$ are overlapped on each image to indicate the location of Nb and Se atoms. (m) Spatial distribution of Se $4p$ orbital charge density with an isovalue of 2×10^{-5} (electron/bohr^3). (n) Spatial distribution of Nb $4d$ orbital charge density with an isovalue of 1×10^{-4} (electron/bohr^3).

the value of tunneling current is 10–100 times larger than ordinary measurement. Thus, it is necessary to consider the effects of the electric field since in some cases, a stronger electric field may affect the electronic structure of TMD materials [47–49] or manipulate CDW phases [50,51]. In order to further investigate the influence of the electric field, we have conducted a DFT calculation to simulate charge distribution with and without a 2 GV/m electric field, which is similar to the order in the STM experiments. As shown in Fig. S6 in the Supplemental Material, the results show that the electric field does not affect the CDW phase or weaken the intensity of CDW. Under this strong electric field, the intensity of 3×3 CDW still remains the same spatial distribution along the c axis. Therefore, the transition and modulation of intensity are not caused by the larger electric field.

F. Relationship with orbital charges

To discuss the origin of this 3D spatial distribution of 3×3 CDW in $NbSe_2$, we further consider the contribution from different orbitals at Se and Nb levels. First of all, Figs. 5(a)–5(f) show the images observed under different tunneling currents by extracting only 1×1 lattice information. By overlapping with the atomic model, it shows that Se sites appear as bright spots at the Se level and become dark spots at the Nb level. This further indicates that we consistently probe the Nb level at 100 nA. Similar results can be obtained while analyzing simulated images by DFT calculation at different heights along the c axis as shown in Figs. 5(g)–5(l). Second, we calculated the orbital-resolved partial charge density (orbital-resolved PCD) near Se and Nb atoms. Figures 5(m) and 5(n) reveal the orbital-resolved PCD distributions of Se $4p$ orbitals and Nb $4d$ orbitals, respectively. The distribution of Se $4p$ orbitals matches the extracted STM image observed at the Se level where most of the orbital charges are located on the Se atoms. Meanwhile, the distribution of Nb $4d$ orbitals shows similarities to the extracted STM image observed at the Nb level. The $4d$ orbitals of neighboring Nb atoms overlap with each other. The orbital-resolved PCD here further indicates that the orbitals in $NbSe_2$ play a key role in modulating the 3×3 charge order and results in the variation of its magnitude as observed in Figs. 3(p) and 3(q); i.e., the magnitude change of 3×3 is due to the contribution of orbital charges from Se p orbitals (Nb d orbitals) decreases (increases) while ramping up the set points. Also, the evolution of spatial distribution as shown in Figs. 4(i) and 4(j) can be attributed to the main contribution to the charge density shifts from Se p orbitals to Nb d orbitals. Therefore, the different distribution of 3×3 CDW at Se and Nb levels mainly arises from the distinct spatial distribution of different orbital charges and the magnitude

of 3×3 CDW is closely connected to the density of these orbital charges.

IV. CONCLUSIONS

By current-dependent STM experiments and DFT calculations, it is found that the 3×3 CDW in $NbSe_2$ exhibits an intriguing spatial distribution extended over the Se and Nb sublayers. Hereby, the modulation of 3×3 CDW along the c axis is analyzed in great detail in conjunction with theoretical calculations. The 3D spatial distribution is clearly visualized by STM and DFT calculation, which is related to the charges dominated by Se $4p$ orbitals and Nb $4d$ orbitals. The CDW basically modulates the orbital charges located at different height levels, resulting in different distributions. On the other hand, the apparent magnitude of the 3×3 CDW is strongly modulated by the distribution of orbital charges. Our results further indicate that the apparent magnitude of the 3×3 CDW is stronger at the height level with larger localized orbital charges; i.e., 3×3 charge order is clearer at height level near the maxima of Se and Nb orbital charges. During submission, we have carried out a similar experiment in other instruments at 10.2 K for higher tunneling currents. The results have shown a similar behavior to the results at 4.8 K. Therefore, this study provides real-space information to further understand the relationship between orbital textures and CDW, which can be applied to other CDW materials in diverse aspects.

ACKNOWLEDGMENTS

This work was financially supported by the National Science and Technology Council of Taiwan, under Grants No. NSTC 110-2112-M-A49-013-MY3, No. NSTC 110-2112-M-A49-022-MY2, No. NSTC 110-2112-M-032-014-MY3, No. NSTC 112-2112-M-A49-029, No. NSTC 112-2923-M-A49-001-MY2, No. NSTC 113-2628-M-A49-006-MY3, No. NSTC 113-2124-M-A49-007, No. NSTC 113-2112-M-032-013, No. NSTC 113-2112-M-027-003, and No. NSTC 114-2112-M-032-009-MY3. Also, it was partially supported by NSTC T-Star center project "Future Semiconductor Technology Research Center" (Grant No. NSTC 114-2634-F-A49-001). The authors also thank the National Center for High-Performance Computing (NCHC) in Taiwan for providing computational resources.

DATA AVAILABILITY

Data for this article, including STM images are available at Open Science Framework at [52].

[1] K. Rossnagel, On the origin of charge-density waves in select layered transition-metal dichalcogenides, J. Phys.: Condens. Matter **23**, 213001 (2011).

[2] K. Cho, M. Kończykowski, S. Teknowijoyo, M. A. Tanatar, J. Guss, P. B. Gartin, J. M. Wilde, A. Kreyssig, R. J. McQueeney, A. I. Goldman, V. Mishra, P. J. Hirschfeld, and R. Prozorov, Using controlled disorder to probe the interplay between charge order and superconductivity in $NbSe_2$, Nat. Commun. **9**, 2796 (2018).

[3] L. J. Li, E. C. T. O'Farrell, K. P. Loh, G. Eda, B. Özyilmaz, and A. H. Castro Neto, Controlling many-body states by the electric field effect in a two-dimensional material, Nature (London) **529**, 185 (2016).

[4] P. Chen, Woei Wu Pai, Y.-H. Chan, A. Takayama, C.-Z. Xu, A. Karn, S. Hasegawa, M. Y. Chou, S.-K. Mo, A.-V. Fedorov, and T.-C. Chiang, Emergence of charge density waves and a pseudogap in single-layer $TiTe_2$, Nat. Commun. **8**, 516 (2017).

[5] H. Ryu, Y. Chen, H. Kim, H.-Z. Tsai, S. Tang, J. Jiang, F. Liou, S. Kahn, C. Jia, A. A. Omrani, J. H. Shim, Z. Hussain, Z.-X. Shen, K. Kim, B.-Il Min, C. Hwang, M. F. Crommie, and S.-K. Mo, Persistent charge-density-wave order in single-layer $TaSe_2$, Nano Lett. **18**, 689 (2018).

[6] D. L. Bolloc'h, S. Ravy, J. Dumas, J. Marcus, F. Livet, C. Detlefs, F. Yakhou, and L. Paolasini, Charge density wave dislocation as revealed by coherent x-ray diffraction, Phys. Rev. Lett. **95**, 116401 (2005).

[7] D. Lin, S. Li, J. Wen, H. Berger, L. Forró, H. Zhou, S. Jia, T. Taniguchi, K. Watanabe, X. Xi, and M. S. Bahramy, Patterns and driving forces of dimensionality-dependent charge density waves in 2H-type transition metal dichalcogenides, Nat. Commun. **11**, 2406 (2020).

[8] D. L. Duong, G. Ryu, A. Hoyer, C. Lin, M. Burghard, and K. Kern, Correction to Raman characterization of the charge density wave phase of 1T-$TiSe_2$: From bulk to atomically thin layers, ACS Nano **11**, 2304 (2017).

[9] T.-R. T. Han, F. Zhou, C. D. Malliakas, P. M. Duxbury, S. D. Mahanti, M. G. Kanatzidis, and C.-Y. Ruan, Exploration of metastability and hidden phases in correlated electron crystals visualized by femtosecond optical doping and electron crystallography, Sci. Adv. **1**, e1400173 (2015).

[10] A. W. Tsen, R. Hovden, D. Wang, Y. D. Kim, J. Okamoto, K. A. Spoth, Y. Liu, W. Lu, Y. Sun, J. C. Hone, L. F. Kourkoutis, P. Kim, and A. N. Pasupathy, Structure and control of charge density waves in two-dimensional 1T-TaS_2, Proc. Natl Acad. Sci. USA **112**, 15054 (2015).

[11] H. Zhao, H. Li, B. R. Ortiz, S. M. L. Teicher, T. Park, M. Ye, Z. Wang, L. Balents, S. D. Wilson, and I. Zeljkovic, Cascade of correlated electron states in the kagome superconductor CsV_3Sb_5, Nature (London) **599**, 216 (2021).

[12] M. Spera, A. Scarfato, Á. Pásztor, E. Giannini, D. R. Bowler, and Ch. Renner, Insight into the charge density wave gap from contrast inversion in topographic STM images, Phys. Rev. Lett. **125**, 267603 (2020).

[13] W.-C. Chiu, S. Mardanya, R. Markiewicz, J. Nieminen, B. Singh, T. Hakioglu, A. Agarwal, T.-R. Chang, H. Lin, and A. Bansil, Strain-induced charge density waves with emergent topological states in monolayer $NbSe_2$, ACS Nano **19**, 18108 (2025).

[14] D. Lin, A. Ranjbar, X. Li, X. Huang, Y. Huang, H. Berger, L. Forró, K. Watanabe, T. Taniguchi, R. V. Belosludov, T. D. Kühne, H. Ding, M. S. Bahramy, and X. Xi, Axial-bonding-driven dimensionality effect on the charge-density wave in $NbSe_2$, Nano Lett. **22**, 9389 (2022).

[15] A. Sanna, C. Pellegrini, E. Liebhaber, K. Rossnagel, K. J. Franke, and E. K. U. Gross, Real-space anisotropy of the superconducting gap in the charge-density wave material 2*H*-$NbSe_2$, npj Quantum Mater. **7**, 6 (2022).

[16] X. Xi, L. Zhao, Z. Wang, H. Berger, L. Forró, J. Shan, and K. F. Mak, Strongly enhanced charge-density-wave order in monolayer $NbSe_2$, Nat. Nanotech. **10**, 765 (2015).

[17] M. Leroux, I. Errea, M. Le Tacon, S.-M. Souliou, G. Garbarino, L. Cario, A. Bosak, F. Mauri, M. Calandra, and P. Rodière, Strong anharmonicity induces quantum melting of charge density wave in 2*H*-$NbSe_2$ under pressure, Phys. Rev. B **92**, 140303(R) (2015).

[18] C. Wen, Y. Xie, Y. Wu, S. Shen, P. Kong, H. Lian, J. Li, H. Xing, and S. Yan, Impurity-pinned incommensurate charge density wave and local phonon excitation in 2*H*-NbS_2, Phys. Rev. B **101**, 241404(R) (2020).

[19] F. Zheng, Z. Zhou, X. Liu, and J. Feng, First-principles study of charge and magnetic ordering in monolayer $NbSe_2$, Phys. Rev. B **97**, 081101(R) (2018).

[20] K. C. Rahnejat, C. A. Howard, N. E. Shuttleworth, S. R. Schofield, K. Iwaya, C. F. Hirjibehedin, Ch. Renner, G. Aeppli, and M. Ellerby, Charge density waves in the graphene sheets of the superconductor CaC_6, Nat. Commun. **2**, 558 (2011).

[21] B. Guster, C. Rubio-Verdú, R. Robles, J. Zaldívar, P. Dreher, M. Pruneda, J. Á. Silva-Guillén, D.-J. Choi, J. I. Pascual, M. M. Ugeda, P. Ordejón, and E. Canadell, Coexistence of elastic modulations in the charge density wave state of 2*H*-$NbSe_2$, Nano Lett. **19**, 3027 (2019).

[22] Y.-X. Jiang, J.-X. Yin, M. M. Denner, N. Shumiya, B. R. Ortiz, G. Xu, Z. Guguchia, J. He, M. S. Hossain, X. Liu, J. Ruff, L. Kautzsch, S. S. Zhang, G. Chang, I. Belopolski, Q. Zhang, T. A. Cochran, D. Multer, M. Litskevich, Z.-J. Cheng *et al.*, Unconventional chiral charge order in kagome superconductor KV_3Sb_5, Nat. Mater. **20**, 1353 (2021).

[23] T. Neupert, M. M. Denner, J.-X. Yin, R. Thomale, and M. Z. Hasan, Charge order and superconductivity in kagome materials, Nat. Phys. **18**, 137 (2022).

[24] G. Zheng, C. Tan, Z. Chen, M. Wang, X. Zhu, S. Albarakati, M. Algarni, J. Partridge, L. Farrar, J. Zhou, W. Ning, M. Tian, M. S. Fuhrer, and L. Wang, Electrically controlled superconductor-to-failed insulator transition and giant anomalous Hall effect in kagome metal CsV_3Sb_5 nanoflakes, Nat. Commun. **14**, 678 (2023).

[25] H. S. Kim, S. Kim, K. Kim, B. I. Min, Y.-H. Cho, L. Wang, S.-W. Cheong, and H. W. Yeom, Nanoscale superconducting honeycomb charge order in $IrTe_2$, Nano Lett. **16**, 4260 (2016).

[26] M. M. Ugeda, A. J. Bradley, Y. Zhang, S. Onishi, Y. Chen, W. Ruan, C. O.-Aristizabal, H. Ryu, M. T. Edmonds, H.-Z. Tsai, A. Riss, S.-K. Mo, D. Lee, A. Zettl, Z. Hussain, Z.-X. Shen, and M. F. Crommie, Characterization of collective ground states in single-layer $NbSe_2$, Nat. Phys. **12**, 92 (2016).

[27] G. Gye, E. Oh, and H. W. Yeom, Topological landscape of competing charge density waves in 2*H*-$NbSe_2$, Phys. Rev. Lett. **122**, 016403 (2019).

[28] Y. Chen, W. Ruan, M. Wu, S. Tang, H. Ryu, H.-Z. Tsai, R. L. Lee, S. Kahn, F. Liou, C. Jia, O. R. Albertini, H. Xiong, T. Jia, Z. Liu, J. A. Sobota, A. Y. Liu, J. E. Moore, Z.-X. Shen, S. G. Louie, S.-K. Mo, and M. F. Crommie, Strong correlations and orbital texture in single-layer 1T-TaS_2, Nat. Phys. **16**, 218 (2020).

[29] Á. Pásztor, A. Scarfato, M. Spera, F. Flicker, C. Barreteau, E. Giannini, J. van Wezel, and C. Renner, Multiband charge density wave exposed in a transition metal dichalcogenide, Nat. Commun. **12**, 6037 (2021).

[30] F. Flicker and J. van Wezel, Charge order from orbital-dependent coupling evidenced by $NbSe_2$, Nat. Commun. **6**, 7034 (2015).

[31] T. Ritschel, J. Trinckauf, K. Koepernik, B. Büchner, M. v. Zimmermann, H. Berger, Y. I. Joe, P. Abbamonte, and J. Geck, Orbital textures and charge density waves in transition metal dichalcogenides, Nat. Phys. **11**, 328 (2015).

[32] H. Kim, Y. Yoshida, C.-C. Lee, T.-R. Chang, H.-T. Jeng, H. Lin, Y. Haga, Z. Fisk, and Y. Hasegawa, Atomic-scale visualization of surface-assisted orbital order, Sci. Adv. **3**, eaao0362 (2017).

[33] P. Hohenberg and W. Kohn, Inhomogeneous electron gas, Phys. Rev. **136**, B864 (1964).

[34] W. Kohn and L. J. Sham, Self-consistent equations including exchange and correlation effects, Phys. Rev. **140**, A1133 (1965).

[35] T. Ozaki, Variationally optimized atomic orbitals for large-scale electronic structures, Phys. Rev. B **67**, 155108 (2003).

[36] T. Ozaki and H. Kino, Efficient projector expansion for the *ab initio* LCAO method, Phys. Rev. B **72**, 045121 (2005).

[37] I. Morrison, D. M. Bylander, and L. Kleinman, Nonlocal Hermitian norm-conserving Vanderbilt pseudopotential, Phys. Rev. B **47**, 6728 (1993).

[38] T. Ozaki and H. Kino, Numerical atomic basis orbitals from H to Kr, Phys. Rev. B **69**, 195113 (2004).

[39] J. P. Perdew, K. Burke, and M. Ernzerhof, Generalized gradient approximation made simple, Phys. Rev. Lett. **77**, 3865 (1996).

[40] J. Tersoff and D. R. Hamann, Theory of the scanning tunneling microscope, Phys. Rev. B **31**, 805 (1985).

[41] K. Momma and F. Izumi, *VESTA:* a three-dimensional visualization system for electronic and structural analysis, J. Appl. Crystallogr. **41**, 653 (2008).

[42] Y.-T. Lee and T. Ozaki, OpenMX Viewer: A web-based crystalline and molecular graphical user interface program, J. Mol. Graph. Model. **89**, 192 (2019).

[43] C. S. Lian, C. Si, and W. Duan, Unveiling charge-density wave, superconductivity, and their competitive nature in two-dimensional $NbSe_2$, Nano Lett. **18**, 2924 (2018).

[44] A. Soumyanarayanan, M. M. Yee, Y. He, J. van Wezel, D. J. Rahn, K. Rossnagel, E. W. Hudson, M. R. Norman, and J. E. Hoffman, Quantum phase transition from triangular to stripe charge order in $NbSe_2$, Proc. Natl Acad. Sci. USA **110**, 1623 (2013).

[45] See Supplemental Material at http://link.aps.org/supplemental/10.1103/dn1j-gkjs for I-Z measurement, the partial charge density distribution of a tungsten tip's apex, the charge density distribution at different Se sites in hollow phase, current-modulated 3×3 CDW intensity of filled phase, the comparison of relative 3×3 CDW intensity as function of current, the DFT simulated STM images under the electric field, Fourier-extracted STM images of 11 lattice at filled phase region under each set point, the partial charge density projected from the top Se and Nb atoms of $NbSe_2$-$3 \times 3 \times 1$ hollow and filled phases, and more current-dependent STM images measured by the other instrument.

[46] N. S. Sivakumar, J. Aretz, S. Scherb, M. V. M. Mavric, N. Huijgen, U. Kamber, D. Wegner, A. A. Khajetoorians, M. Rösner, and N. Hauptmann, Influence of surface relaxations on scanning probe microscopy images of the charge density wave material 2*H*-$NbSe_2$, Phys. Rev. B **111**, 075409 (2025).

[47] M.-K. Lin, G.-H. Chen, C.-L. Ho, W.-C. Chueh, J. A. Hlevyack, C.-N. Kuo, T.-Y. Fu, J.-J. Lin, C. S. Lue, W.-H. Chang, N. Takagi, R. Arafune, T.-C. Chiang, and C.-L. Lin, Tip-mediated bandgap tuning for monolayer transition metal dichalcogenides, ACS Nano **16**, 14918 (2022).

[48] N. E. Staley, J. Wu, P. Eklund, Y. Liu, L. Li, and Z. Xu, Electric field effect on superconductivity in atomically thin flakes of $NbSe_2$, Phys. Rev. B **80**, 184505 (2009).

[49] F. Liu, J. Zhou, C. Zhu, and Z. Liu, Electric field effect in two-dimensional transition metal dichalcogenides, Adv. Funct. Mater. **27**, 1602404 (2017).

[50] X. Song, L. Liu, Y. Chen, H. Yang, Z. Huang, B. Hou, Y. Hou, X. Han, H. Yang, Q. Zhang, T. Zhang, J. Zhou, Y. Huang, Y. Zhang, H.-J. Gao, and Y. Wang, Atomic-scale visualization of chiral charge density wave superlattices and their reversible switching, Nat. Commun. **13**, 1843 (2022).

[51] X. Ma, T. Dai, S. Dang, S. Kang, X. Chen, W. Zhou, G. Wang, H. Li, P. Hu, Z. He, Y. Sun, D. Li, F. Yu, X. Zhou, H. Chen, X. Chen, S. Wu, and S. Li, Charge density wave phase transitions in large-scale few-layer 1T-VTe_2 grown by molecular beam epitaxy, ACS Appl. Mater. Interfaces **11**, 10729 (2019).

[52] C. Lin, $NbSe_2$ Tomography (2024), https://osf.io/hbqup/overview?view_only=8766af69c0a44ac5b0491ac5b540c5f9.

Correction: Contact author footnotes have been added for the last four authors.